Chemical Engineering Journal 524 (2025) 168879

Contents lists available at ScienceDirect

Chemical Engineering Journal

journal homepage: www.elsevier.com/locate/cej

# Gradient hydrogen bonding and π–π interactions: A dual-mechanism binder for resilient and high-performance silicon-based anodes

Yumi Kang [a,d,1], Ji Seong Heo [b,d,1], Jong Hyeok Han [a,d], Jun Won Heo [b,d], Daniel Yim [c,e], Doo Ho Kim [c,e], Seo Jin Yeon [a,d], Sae Chan Yoon [b,d], Hyungjun Kim [c,e,*], Taeeun Yim [b,d,**], Tae-Hyun Kim [a,d,**]

[a] Organic Material Synthesis Laboratory, Department of Chemistry, Incheon National University, Incheon, 22012, Republic of Korea
[b] Advanced Batteries Laboratory, Department of Chemistry, Incheon National University, Incheon, 22012, Republic of Korea
[c] Quantum Chemistry Laboratory, Department of Chemistry, Hanyang University, Seoul, 04763, Republic of Korea
[d] Research Institute of Basic Sciences, Incheon National University, Incheon, 22012, Republic of Korea
[e] Research Institute of Natural Science, Hanyang University, Seoul, 04763, Republic of Korea

ARTICLE INFO

*Keywords:*
Polydopamine–glutathione additive
Multifunctional binder
Si anode
Gradient hydrogen bond
π–π interactions

ABSTRACT

Polydopamine–glutathione (PDG) is mixed with carboxymethyl cellulose (CMC) to synthesize a new functional CMC–PDG binder. PDG additive significantly improves the mechanical strength, adhesiveness, and elasticity of the corresponding electrode compared with a pristine CMC binder. This is due to the multiple hydrogen-bonding groups in PDG, which form strong interactions with Si and CMC, effectively dispersing the internal stress caused by the volume expansion of Si. The Si electrode containing CMC–PDG binder exhibits greater capacity retention, and a superior cycle life compared with CMC in both $SiO_x$ and Si/C composite electrodes. When applied to $SiO_x$ electrode, the CMC-PDG-based electrode achieves a high capacity retention of 72.6 % after 100 cycles. Density functional theory and noncovalent interaction simulations confirm that PDG forms hydrogen bonds with Si and CMC and strengthens π–π interactions with graphite and styrene–butadiene rubber. In addition, full-cell with high loading density electrodes shows a high capacity retention of 68.5 % after 300 cycles for the CMC–PDG electrode. This new binder is a key technology for high-performance Si-based anodes at low cost through a simple manufacturing process and is expected to accelerate the commercialization of next-generation high-energy-density lithium-ion batteries.

## 1. Introduction

Lithium-ion batteries (LIBs) are currently the key driving force behind advances in the battery market, as their application has extended beyond small portable devices, such as smartphones and smartwatches, to electric vehicles, energy storage devices, and other large-scale electronic systems. However, demand remains high for electric vehicles capable of long-distance travel and high-speed charging, which require LIBs with higher energy density. Owing to its high theoretical capacity (4200 mAh $g^{-1}$), Si can meet such needs, garnering significant attention as a promising advanced anode material, which is a prerequisite for high-energy-density LIBs [1–3].

The practical application of Si anodes has been limited by factors including the severe volume changes that occur in Si during the repeated charge–discharge of $Li^+$ ions, the resulting pulverization of Si particles and their delamination from the current collector, and the formation of an unstable solid electrolyte interface (SEI). At the current level of technology, rather than being solely employed as an anode active material, Si is often used in Si/C composites that partially incorporate Si into graphite, typically with a mix ratio of 10 % or less. These composites may achieve a capacity more than twice that of commercial graphite anodes; however, they fail to meet the needs of high-energy-density LIBs. Therefore, it is essential to further increase the Si content, ultimately even to 100 %. To this end, the high stress generated in Si during its alloying with $Li^+$ ions must be effectively addressed [4–8].

Several researchers have proposed strategies to achieve novel Si

* Correspondence to: Department of Chemistry, Hanyang University, Seoul, 04763, Republic of Korea.
** Corresponding authors at: Department of Chemistry, Incheon National University, Incheon, 22012, Republic of Korea.
*E-mail addresses:* kimhyungjun@hanyang.ac.kr (H. Kim), yte0102@inu.ac.kr (T. Yim), tkim@inu.ac.kr (T.-H. Kim).
[1] equally contributed to this work.

https://doi.org/10.1016/j.cej.2025.168879
Received 30 June 2025; Received in revised form 8 September 2025; Accepted 23 September 2025
Available online 25 September 2025

anodes with improved durability and stability, such as by employing nanosize Si [9,10], applying an interfacial coating to Si [11,12], and functionalizing or modifying polymer binders capable of interacting with Si particles [13,14]. In particular, the application of functional binders is considered the most affordable and effective strategy for mitigating the excessive volume changes observed in Si anodes while maintaining their structural integrity [15,16].

Despite accounting for a relatively small proportion of the total electrode mass (preferably with a content of no more than 5 %), binders play a critical role in keeping the active material, conductive material, and current collector in contact. Among the widely used commercial polymer binders for Si anodes are poly(acrylic acid) (PAA) [17–19] and carboxymethyl cellulose (CMC) [20–22]. These binders contain many polar functional groups, such as -OH and -COOH, which not only help them effectively interact with Si by forming hydrogen bonds but also allow them to dissolve easily in water. These characteristics enable an eco-friendly electrode manufacturing process using water as the solvent.

CMC, along with styrene–butadiene rubber (SBR), is widely used as a binder for Si anodes. They are often combined to compensate for each other's limitations. More specifically, while CMC serves as a thickener, improving mechanical properties such as hardness, SBR enhances adhesion and elastic properties and facilitates graphite dispersion, exhibiting remarkable stability in Si/C composite anodes [23,24]. However, even with the application of these binders, excessive volume expansion remains a problem when the Si content is high or pure Si is used as an anode, hindering the commercialization of Si-based anodes.

Most functional binders have been developed by enhancing the stability of a linear polymer with excellent mechanical hardness, such as CMC or PAA, through chemical or physical crosslinking, to help them accommodate the volume expansion of Si more effectively [25–27]. In addition, conductive binders based on novel polymers [28], three-dimensional network binders [29] and self-healing binders [30] have also been developed to further enhance electrode performance and long-term stability. However, while polymer binders enhanced through a network of crosslinked structures exhibit improved resistance and mechanical stability against the volume expansion of Si, they may excessively increase the hardness of the resulting anodes, particularly in thicker anodes or when Si with a large particle size is used. In this case, the anode may undergo excessive stress and structural degradation, resulting in unreliable cell performance under the harsh conditions required for commercialization.

There is therefore growing demand for advanced binders that combine mechanical strength with ductility and elasticity, because elastic polymer binders can more effectively accommodate the volume expansion of Si while mitigating the internal stress experienced by the Si anodes during a cycle. These binders are known to operate more reliably, even under the harsh conditions [31–34].

In this study, PDA–GT (PDG), a novel functional binder additive, was developed by chemically integrating polydopamine (PDA), which contains polar catechol groups, with glutathione (GT), a natural biomolecule derived from amino acids that includes multiple hydrogen-bonded functional groups. PDG was then added to carboxymethyl cellulose (CMC), one of the most widely used aqueous binders, to obtain CMC–PDG. The PDG was synthesized through a simple process involving the in situ polymerization of dopamine (DP), followed by the thiol-Michael addition reaction between PDA and GT. The resulting PDG interacts with Si and CMC through its multiple hydrogen bonds and polar functional groups. Moreover, the numerous hydrogen bonds formed between OH groups on the surface of the additive, CMC, and Si tend to dissociate in a sequential order based on binding strength during charge–discharge cycles, more effectively mitigating and dissipating the stress caused by the volume expansion of Si.

Furthermore, the PDG improves the elasticity and adhesion of CMC and engages in π–π interactions with graphite and SBR, reliably maintaining the mechanical properties of the resulting electrode. These enhanced characteristics demonstrate its high potential for use in Si-based composite active materials (including $SiO_x$ and Si/C) as a versatile binder for Si anodes (Fig. 1).

In this study, the amount of PDG added was adjusted to optimize the CMC–PDG binder content. The obtained binders were applied to both $SiO_x$-based electrodes and Si/C composite electrodes, and their effect on the mechanical and electrochemical properties of the electrodes was examined by comparison with CMC, a commercial binder. Additionally, simulations were conducted to confirm that the additives could interact with Si, graphite, and SBR in practice. Full-cell evaluations and electrode analyses, particularly at the commercialization level, were also performed to assess the feasibility of these CMC–PDG binders for commercialization.

## 2. Experimental section

### 2.1. Materials

Dopamine hydrochloride (DA) and potassium hydroxide (KOH) were purchased from Sigma-Aldrich (St. Louis, MO, USA). GT was purchased from TCI (Tokyo, Japan). CMC, silicon oxide ($SiO_x$), Si/C, Super C powder, and the electrolyte were all provided by Hyundai Motor Company.

### 2.2. Synthesis of polydopamine–glutathione additive

First, 100 mg of DA and 100 mg of GT were added to 20 mL of pH 8.5 KOH solution, and the solution was stirred for 24 h at room temperature in the dark, during which it turned brown [35]. The additives synthesized this way were named 11PDG, 21PDG, and 12PDG, depending on their weight percent ratio of DA to GT.

### 2.3. Binder solution preparation and electrode fabrication

To prepare a CMC aqueous solution, 2 g of CMC was dissolved in 150 mL of distilled water and mixed with the synthesized PDG solution. This mixture was stirred at 70 °C for 4 h to obtain the CMC–PDG binder solution.

For half-cell tests, $SiO_x$, Super C, and a polymer binder (8:1:1 mass ratio) were dispersed in distilled water. The slurry was cast using the doctor blade technique, with a mass loading of 1.5 to 2.5 mg $cm^{-2}$ onto copper foil. Electrodes containing Si/C were also prepared using the same procedure, with a loading of 1.5 mg $cm^{-2}$. The prepared electrodes were dried for 10 min at 120 °C in an oven before being roll-pressed to improve the packing density. Subsequently, the electrodes were roll-pressed to achieve a composite density of 1.1–1.3 g $cm^{-3}$, punched into 12 φ-sized, and further dried at 120 °C for 10 h to remove residual water. Thereafter, the electrodes were assembled into half-cells using Li metal as the counter electrode. The cells were aged for 12 h and charged–discharged in the voltage range from 0.01 to 1.6 V, in increments of 0.1C for three cycles and increments of 0.5C and 1.0C.

In assembling the full-cells, the anodes and cathodes were prepared as follows. Regarding the anode, the mixture of the anode materials (10.8 g of graphite, 0.6 g of $SiO_x$, and 0.6 g of Si/C in a mass ratio of 9.0:0.5:0.5), Super C, and each binder (mass ratio of 95.8:2.9:1.3) was dispersed in 12.9 mL of distilled water, and the resulting mixture was further stirred for 30 min. The well-dispersed anode slurries were then coated onto the Cu current collector and dried at 80 °C for 10 min. The loading density and electrode density of the anode were 8.0 mg $cm^{-2}$ and 1.6 g $cm^{-3}$, respectively. Regarding the cathode, 1.8 g of the NCM83 cathode material ($LiNi_{0.83}Co_{0.12}Mn_{0.05}O_2$), 0.1 g of Super C, and 0.1 g of the polyvinylidene difluoride binder were dispersed in 1.5 mL of *N*-methyl pyrrolidone. The mixture was further stirred for 30 min, and the resulting slurries were coated onto the Al current collector. Subsequently, the NCM83 cathode was dried at 120 °C for 3 h and further dried at 120 °C for 12 h in a vacuum oven. The loading density and electrode density of the cathode were 17.1 mg $cm^{-2}$ and 3.0 g $cm^{-3}$,

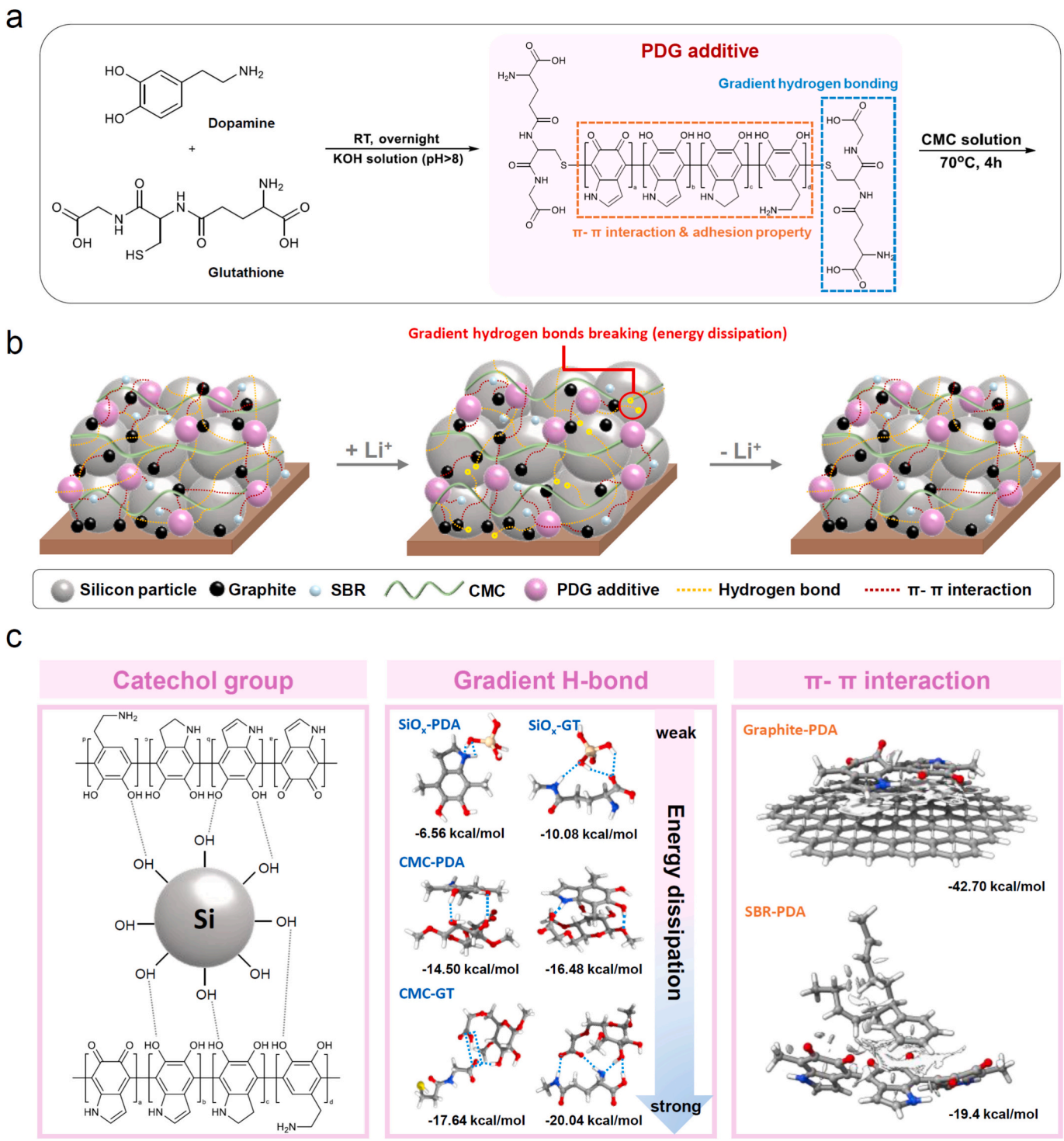


**Fig. 1.** (a) Chemical structure of synthesized PDG additive. (b) Lithiation/delithiation of Si-based anode with CMC–PDG binder. (c) Functions of CMC–PDG binder.

respectively. In assembling the full-cells, 12 φ-sized electrodes were dried at 120 °C for 10 h under vacuum to remove residual water. The negative-to-positive capacity ratio was fixed at 1.05. The cells were aged for 12 h and charged/discharged in the voltage range of 3.0 to 4.2 V, in increments of 0.1C for three cycles and increments of 2.0C for 300 cycles at 45 °C.

### 2.4. Characterization and measurement of material properties

Fourier transform infrared spectroscopy (FT-IR) spectra were acquired using a Spectrum Two FT-IR spectrometer with an attenuated total reflectance accessory (PerkinElmer) to examine the changes in the functional groups and bonds. The dispersion of the solution was measured using a zeta potential analyzer (ELS-Z) with a polymer binder solution containing 0.001 wt% $SiO_x$, under a voltage range of −100 to 100 mV and a current range of 0 to 50 mA. A rheometer (ARES-G2) was used to measure the viscoelastic behavior. A dynamic mechanical analyzer (DMA, DMA7100) was used to measure the glass transition temperature. The electrodes were prepared with 12-mm 3 M tape used for the peel test. A universal testing machine (Shimadzu) was used to

measure the mechanical properties and the adhesion of the silicon and Super C to the polymeric binder at a constant displacement rate of 20 mm $min^{-1}$. A nanoindentation test was performed using an iNano nanoindenter (KLA-instrument). The indenter tip was pressed onto the specimen surface under a maximum pressing force of 0.8 mN, and the depth of the resulting indentation was used to determine the hardness of each electrode. The modulus was determined by measuring the force required for the specimen to recover to its original shape while removing the indenter tip.

The fracture toughness was evaluated via a pure shear test. The CMC and CMC-PDG binders were fabricated with the following dimensions: width ($a_0$) = 20 mm and thickness ($b_0$) = 0.1 mm. The mechanical work, denoted as W(H), was calculated as the area under the force–displacement curve. During testing, the samples were subjected to tensile loading to the point of crack propagation and ultimate failure. The fracture toughness ($\Gamma$) was subsequently calculated based on the critical crack extension distance ($H_c$) using the relation $\Gamma = W(H_c)/a_0b_0$.

The morphology of all the electrodes before and after cycling was analyzed using a field-emission scanning electron microscope (FE-SEM, IT-800, JEOL). The surface morphology and height variation of the uncompressed Si/C electrodes were characterized using 3D-surface confocal laser scanning microscope (3D-LSM, OLS5100). After cycling, depth profiles of the anodes were collected by time-of-flight secondary ion mass spectrometry (TOF-SIMS) (TOF-SIMS5, ION TOF) at a 50 μm raster size (field of view: 50 μm × 50 μm). To monitor the internal pressure during the discharging step, laboratory-built pressure-potential cells were assembled using each anode, Li metal, electrolyte, and separator. The in situ pressure cells were then discharged from 1.6 V (vs. $Li/Li^+$) to 0.01 V (vs. $Li/Li^+$) at 0.2C and 45 °C, and changes in the internal pressure were recorded as a function of the discharging time until the cell potential reached 0.01 V (vs. $Li/Li^+$).

### 2.5. Characterization and measurement of electrochemical properties

A 2032-type coin cell was used to test the electrochemical performance in an argon-filled glove box. Porous polyethylene (Celgard 2400) was used as the separator, and lithium metal disks were used as the counter and reference electrodes.

Using a CPS-Lab battery cycler (BaSyTec) at 27 °C in a temperature-controlled chamber, all cells were charged to 0.01 V (vs. $Li/Li^+$) by the constant-current/constant-voltage technique and discharged to 1.5 V (vs. $Li/Li^+$) by the constant-current method ($SiO_x$, Si/C electrode: 1C = 1400 mAh $g^{-1}$). Electrochemical impedance spectroscopy (EIS), cyclic voltammetry (CV) and galvanostatic intermittent titration technique (GITT) were performed using an electrochemical potentiostat/galvanostat system (VSP, Bio-Logic). EIS spectra were obtained at an AC amplitude of 10 mV over the frequency range of 100 kHz to 10 MHz, and CV was conducted at a scanning rate of 0.1 mV/s. GITT tests were performed in the range of 0.01 V to 1.6 V, with measurements taken during a 10-min pulse and a 30-min rest period. Lithium diffusion coefficients using scan rate were calculated using the equation 1:

$$D_{Li} = \frac{4}{\pi\tau}\left(\frac{n_m V_m}{S}\right)^2\left(\frac{\Delta E_s}{\Delta E_t}\right)^2 \quad (1)$$

where $\tau$ is the galvanic titration time, $n_m$ is the number of mole, $V_m$ is the molar volume, S is the electrode area, $\Delta E_s$ is total voltage change due to the pulse, $\Delta E_t$ is Voltage change during constant current charging/discharging. Interfacial resistance was measured using an interfacial resistance analyzer (HIOKI, RM2610). Note that the interfacial resistance analyzer quantitatively evaluates the electrode resistance, which can vary depending on the electrode materials (active material, binder materials, and conductive agent), composition, and casting conditions; a lower value indicates a lower resistance.

### 2.6. Simulation information and details

All molecular structures, except for the graphite and $SiO_x$ layers, were initially optimized using the GFN2-xTB method implemented in the xTB package, a semi-empirical approach well-suited for efficient electronic structure predictions in large-scale systems. Further geometry optimizations and electronic energy calculations were carried out at the CAM-B3LYP-D3(BJ)/6–311 + G(d,p)//CAM-B3LYP-D3(BJ)/6-31G(d,p) level of theory using the Gaussian16 software. CAM-B3LYP-D3(BJ) is a range-separated hybrid functional incorporating Grimme's D3(BJ) dispersion correction for improved treatment of intermolecular dispersion interactions.

Non-covalent interactions, including π-π stacking and other weak interactions, were analyzed using the Multiwfn program. Hydrogen bond energies were determined via its topology analysis function, while the visualization of these interactions was achieved through the Non-Covalent Interaction (NCI) analysis module.

## 3. Results and discussion

### 3.1. Characterization of PDA-GT and CMC–PDG

PDG, an additive composed of PDA and GT, was synthesized through the oxidative self-polymerization of DA, followed by the thiol-Michael addition reaction between GT and the resulting PDA (Fig. S1). The weight ratio of DA to GT was fixed at 1:1, and the resulting PDA–GT additive was named 11PDG. 11PDG was then added to CMC at a content of 10 wt%, and the resulting binder was named CMC–11PDG-10.

Comparative spectroscopy was performed to examine the structures of the additive 11PDG and the binder CMC–11PDG-10 based on their FT-IR spectra and to compare them with those of GT and CMC. In 11PDG, the -SH stretching vibration peak, which was originally observed at 2525 $cm^{-1}$ in the pristine GT, was absent, demonstrating that the -SH group of GT had effectively reacted with the PDA [35]. Instead, strong absorption peaks attributed to the stretching vibrations of the -OH and -NH functional groups, characteristic of PDA, were detected at 3200–3500 $cm^{-1}$, with the same phenomenon observed in CMC–11PDG-10. Moreover, the $-COO^-$ peaks (1595 and 1418 $cm^{-1}$) and C-O-C peak (1060 $cm^{-1}$) observed in CMC also appeared in CMC–11PDG-10, confirming the successful integration of 11PDG into CMC (Fig. 2a).

As described above, during the synthesis of 11PDG, PDA was first produced through the oxidative self-polymerization of DA; however, its material structure is not well understood, making its analysis challenging. Therefore, in this study, the UV–Vis absorption spectra of CMC–11PDG-10 were measured from 200 to 800 nm to detect the formation of PDA in the 11PDG additive, and the results were compared with those obtained for neat CMC. In a solution containing CMC–11PDG-10 with added 11PDG, the characteristic peak of PDA was observed at 280 nm, unlike in the case of CMC alone, as shown in Fig. 2b [36]. This observation was attributed to π–π interactions among the aromatic functional groups of PDA, confirming the self-polymerization of DA during the synthesis of 11PDG.

Next, the glass transition temperatures ($T_g$) of CMC–11PDG-10, CMC-21PDG-10 and CMC were measured using a DMA. Both CMC-11PDG-10 and CMC–21PDG-10 exhibited a significantly lower $T_g$ (64.9 °C and 70.8 °C, respectively) than CMC (121.6 °C) (Fig. 2c). This result is due to hydrogen-bonding functional groups in the PDG additive contributing to the formation of noncovalent hydrogen bonds with different binding energies between CMC and PDG. These bonds may weaken the interactions between the polymer chains [37–39]. This implies that PDG serves as a plasticizer within the polymer structure. Additionally, the $T_g$ values were also determined using the storage modulus (E′) from the DMA analysis, and compared with that of CMC (Fig. S2). Consistent with the trends observed in the loss modulus (E″) results, CMC–11PDG-10 and CMC-21PDG-10 exhibited lower $T_g$ values of 57.9 °C and 69.1 °C, respectively, compared to CMC (117.4 °C). These findings further

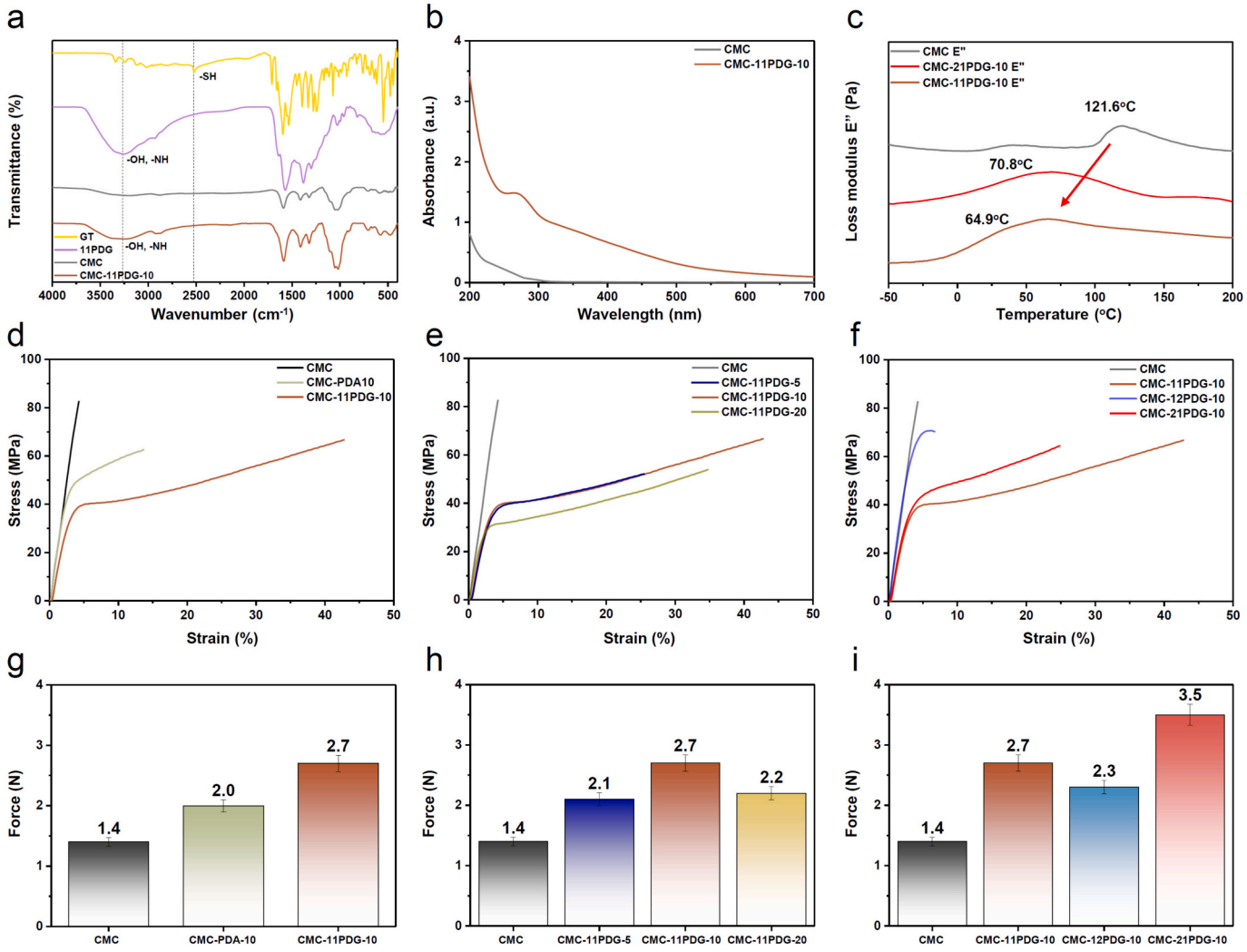


**Fig. 2.** (a) FT-IR, (b) UV–Vis, and (c) DMA spectra of CMC–PDG binder; (d–f) stress–strain curves of different binder films; (g–i) peel-off test results of different binder $SiO_x$ electrode.

support that the PDG additive functions as a plasticizer within the polymer matrix, reducing the glass transition temperature.

Introducing the 11PDG additive reduced the crystallinity of the CMC, increasing the strain capacity of the resulting CMC–11PDG-10 binder [40]. To confirm this, CMC–11PDG-10 was processed into a film, then its stress–strain curve was obtained and compared with that of CMC (Fig. 2d). The CMC film exhibited a high stress of 83 MPa but lacked flexibility. In contrast, the CMC–11PDG-10 film, which included the 11PDG additive (with a DA-to-GT weight ratio of 1:1), showed an approximately 42.9 % increase in strain while maintaining its stress at a comparable level to that of CMC. This improvement was only achieved when PDG, the additive composed of DA and GT, was employed. In the case of the CMC–PDA-10 film, where only PDA was added to CMC with the same content (10 wt%), the increase in strain was limited to 13.7 %. These results can be explained by the formation of hydrogen bonds between 11PDG and CMC through multiphase dissipation mechanisms [41–43], consistent with the interpretation of the $T_g$ data. These data imply that this enhancement is maximized only when both GT and PDA are present. In addition, the toughness of the CMC-11PDG-10 binder was calculated from the stress–strain curves and compared with that of CMC and CMC-PDA-10 (Fig. S3). The toughness values of CMC and CMC-PDA-10 were 1.8 and 6.8 $MJ{\cdot}m^{-3}$, respectively, whereas CMC-11PDG-10 exhibited a markedly enhanced toughness of 20.8 $MJ{\cdot}m^{-3}$. These results indicate that the CMC-11PDG-10 binder can effectively accommodate the mechanical stress associated with the volume expansion of the silicon active material, helping preserve the structural integrity of the electrode and, thereby, contributing to improved long-term battery stability.

Next, $SiO_x$ (the active material), CMC–11PDG-10, and Super C were mixed at an 8:1:1 ratio to fabricate an electrode denoted as ($SiO_x$)CMC–11PDG-10. The adhesion performance of CMC–PDA-10 as the binder was evaluated using this electrode, and the results were compared with those for pristine CMC [denoted as ($SiO_x$)CMC] and ($SiO_x$)CMC–PDA-10, an electrode fabricated by adding PDA to CMC under the same experimental conditions (Fig. 2g).

The adhesion increased in the order ($SiO_x$)CMC (1.4 N) < ($SiO_x$)CMC–PDA-10 (2.0 N) < ($SiO_x$)CMC–11PDG-10 (2.7 N). This result demonstrates that adding 11PDG, which contains both polar catechol groups from PDA and hydrogen-bonding sites present in GT, maximized the interaction between CMC and $SiO_x$, improving the adhesion of the resulting electrodes [44–48].

The electrochemical performance of ($SiO_x$)CMC–11PDG-10, an electrode with $SiO_x$ as the active material, was analyzed and compared with those of ($SiO_x$)CMC and ($SiO_x$)CMC–PDA-10, which used CMC and CMC–PDA-10 as the binder, respectively (Fig. S4a). Even at a high charge–discharge rate of 1C, ($SiO_x$)CMC–11PDG-10 exhibited remarkable capacity retention of 85 % after 50 cycles. In contrast, the capacity retention of ($SiO_x$)CMC–PDA-10, which lacked PDG, was limited to 63

%, although it was higher than that of ($SiO_x$)CMC (40 %). This difference is thought to result from the enhanced adhesion through the synergy between the multiple hydrogen-bonding functional groups of GT in the PDG additive and the polar catechol groups of PDA. This result confirms that adding the PDG additive improved the limited flexibility and adhesion of CMC.

### 3.2. Mechanical properties and electrochemical performance of CMC–PDG with different amounts of PDG additive

The mechanical and electrical properties of CMC were improved by adding 10 wt% PDG. Next, the PDG content was varied to 5, 10, and 20 wt%, yielding three binders with different PDG contents: CMC–11PDG-5, CMC–11PDG-10, and CMC–11PDG-20. Using these binders, electrodes with different PDG contents, denoted as ($SiO_x$)CMC–11PDG-*m* (where *m* is the PDG content), were fabricated under the same experimental conditions as ($SiO_x$)CMC–11PDG-10. Their mechanical and electrochemical characteristics were then compared with those of ($SiO_x$)CMC–11PDG-10 (Fig. 2e, h, and S4b).

The resulting binders with different additive contents were processed into films, and their stress–strain curves were examined. All binders containing the 11PDG additive exhibited a higher strain than CMC, regardless of the 11PDG content. In particular, the strain significantly increased up to an 11PDG content of 10 wt%. However, CMC–11PDG-20, with a PDG content of 20 wt%, exhibited lower stress and strain than CMC–11PDG-10. This was attributed to the excessive amount of PDG additive, which led to aggregation. This trend in the mechanical properties of the binders with different additive contents aligned with the adhesion and cell performances of the $SiO_x$ electrodes fabricated using the same binders (Fig. 2h and S4b). More specifically, the adhesion of the electrodes increased in the order ($SiO_x$)CMC (1.4 N) < ($SiO_x$)CMC–11PDG-5 (2.1 N) < ($SiO_x$)CMC–11PDG-20 (2.2 N) < ($SiO_x$)CMC–11PDG-10 (2.7 N), indicating that the best adhesion performance was achieved when the PDG11 content was 10 wt% (Fig. 2h).

Moreover, their electrochemical performances showed a similar trend to the mechanical test results; ($SiO_x$)CMC–11PDG-10 exhibited the highest capacity retention at 85 %. In contrast, due to the limited amount of PDG additive, ($SiO_x$)CMC–11PDG-5 exhibited a low capacity retention of 40 %, comparable to that of ($SiO_x$)CMC, demonstrating its failure to effectively mitigate the stress caused by the volume expansion of Si. Meanwhile, ($SiO_x$)CMC–11PDG-20 experienced slurry aggregation due to its excessive additive content, hindering uniform casting during electrode fabrication. As a result, its capacity retention was only 53 % (Fig. S4b).

Overall, ($SiO_x$)CMC–11PDG-10, with an optimal 11PDG binder content of 10 wt% relative to CMC, achieved the highest adhesion performance and capacity retention. As such, this composition was subjected to further experiments (Fig. 2h and S4b).

### 3.3. Mechanical properties and electrochemical performance of CMC–PDG binders with different PDG additive monomer ratios

Next, the ratio of the two monomers, DA and GT, in the PDG additive was varied while fixing the PDG content relative to CMC at 10 wt% to determine the optimal composition of the PDG additive (Fig. 2f, i and S4c). In addition to the previously tested 1:1 ratio, the weight percent ratio of DA to GT was adjusted to 1:2 and 2:1. The obtained additives were denoted as 12PDG and 21PDG, respectively. Each additive was added to CMC at 10 wt% and then processed into a film. The mechanical characteristics of the two fabricated binders, CMC–12PDG-10 and CMC–21PDG-10, were analyzed based on their stress–strain curves, and the results were compared with those for CMC–11PDG-10 (Fig. 2f). In CMC–12PDG-10, no significant improvement in strain was observed, indicating that the additive failed to enhance the limited strain performance of CMC. This is attributed to the excess GT present, which induces the DA to engage in the thiol-Michael addition reaction with GT before self-polymerizing into PDA. In contrast, in CMC–21PDG-10, the DA content exceeds that of GT. Consequently, adding polar catechol groups to the additive improves stress and adhesion, even when compared with CMC–11PDG-10, although the strain is slightly reduced as a trade-off (Fig. 2f and i).

The electrochemical properties of ($SiO_x$)CMC–12PDG-10 and ($SiO_x$)CMC–21PDG-10, fabricated using the binders CMC–12PDG-10 and CMC–21PDG-10, respectively, were evaluated, and the results were compared with those of ($SiO_x$)CMC–11PDG-10, which demonstrated the best cell performance among the 11PDG-based electrodes (Fig. S4c). ($SiO_x$)CMC–21PDG-10 exhibited similar behavior to ($SiO_x$)CMC–11PDG-10 up to the 50th cycle. However, above this number of cycles, ($SiO_x$)CMC–21PDG-10 exhibited higher capacity retention than ($SiO_x$)CMC–11PDG-10. This is due to the higher DA content of the CMC–21PDG-10 binder, which increased the number of polar catechol groups. Therefore, improved stress and adhesion performance could be achieved even though the strain remained comparable to that of CMC–11PDG-10. These results confirm that the best mechanical properties and cell performance were achieved in ($SiO_x$)CMC–21PDG-10, which contained 10 wt% CMC–21PDG-10, a binder with the optimal DA: GT ratio of 2:1.

### 3.4. Density functional theory simulation of gradient hydrogen bonding

The gradient hydrogen bonding between the PDG (that is composed of PDA and GT) and CMC and between PDG and $SiO_x$ was analyzed using density functional theory (DFT) [49,50]. For this, PDG was divided into PDA and GT, which constitute PDG, and the interactions with CMC and $SiO_x$ were calculated, respectively. (Fig. 3, Tables S1–5).

Simple molecular models were established for CMC, PDA, GT, and $SiO_x$ and structurally optimized before calculating the CMC–PDA, CMC–GT, $SiO_x$–CMC, $SiO_x$ –PDA, and $SiO_x$ –GT interactions for the compositions of interest [51]. From the results, the binding energy of the hydrogen bonds formed between the components of the additive (PDA or GT) and the active material (CMC or $SiO_x$) was estimated. PDA and GT formed multiple hydrogen bonds with CMC, such as N···OH, O···NH, OH···O, O···OH, OH···N, and NH···O, in broad energy ranges of −1.3 to −16.5 kcal/mol and − 1.3 to −20.0 kcal/mol, respectively (Fig. 3a, Table S1–2). PDA and GT also formed hydrogen bonds of different strengths with $SiO_x$, such as OH···N, O···OH, OH···O, and O···NH, in energy ranges of −1.0 to −10.2 kcal/mol and − 1.9 to −10.1 kcal/mol, respectively (Fig. 3b, Table S3–4). These results demonstrate that the PDG additive forms gradient hydrogen bonds in different forms with CMC and $SiO_x$. Consequently, it achieves greater adhesion, mechanical strength, and flexibility than CMC, as previously confirmed from the mechanical test results. By contrast, CMC formed limited types of hydrogen bonds with $SiO_x$ (O···OH and OH···O) in a relatively narrow energy range of −2.3 to −8.5 kcal/mol (Table S5). These results suggest that adding PDG to CMC increases the number of hydrogen-bonding sites with varying binding energies, resulting in the sequential dissociation of hydrogen bonds in order of binding strength and thus mitigating the stress exerted on the Si anode. Thus, introducing the PDG additive improves the mechanical properties of the binder and enhances the interaction between the binder and the active material. This enables multiphase energy dissipation, mitigating the stress caused by the volume expansion of Si, as demonstrated in the simulations [52–54].

### 3.5. Dispersion stability and viscoelastic behavior of CMC–21-PDG-10

The zeta potential of the electrode slurry was measured to assess its dispersion stability. Generally, an electrode slurry is considered to have excellent dispersion stability when its zeta potential ranges from −40 to −60 [55,56]. CMC and CMC–PDG21–10 had zeta potentials of −61.11 and − 58.85 mV, respectively, indicating that PDG disperses well in CMC without aggregation. The slightly lower absolute value of the zeta potential of CMC–21PDG-10 than that of CMC further confirms the

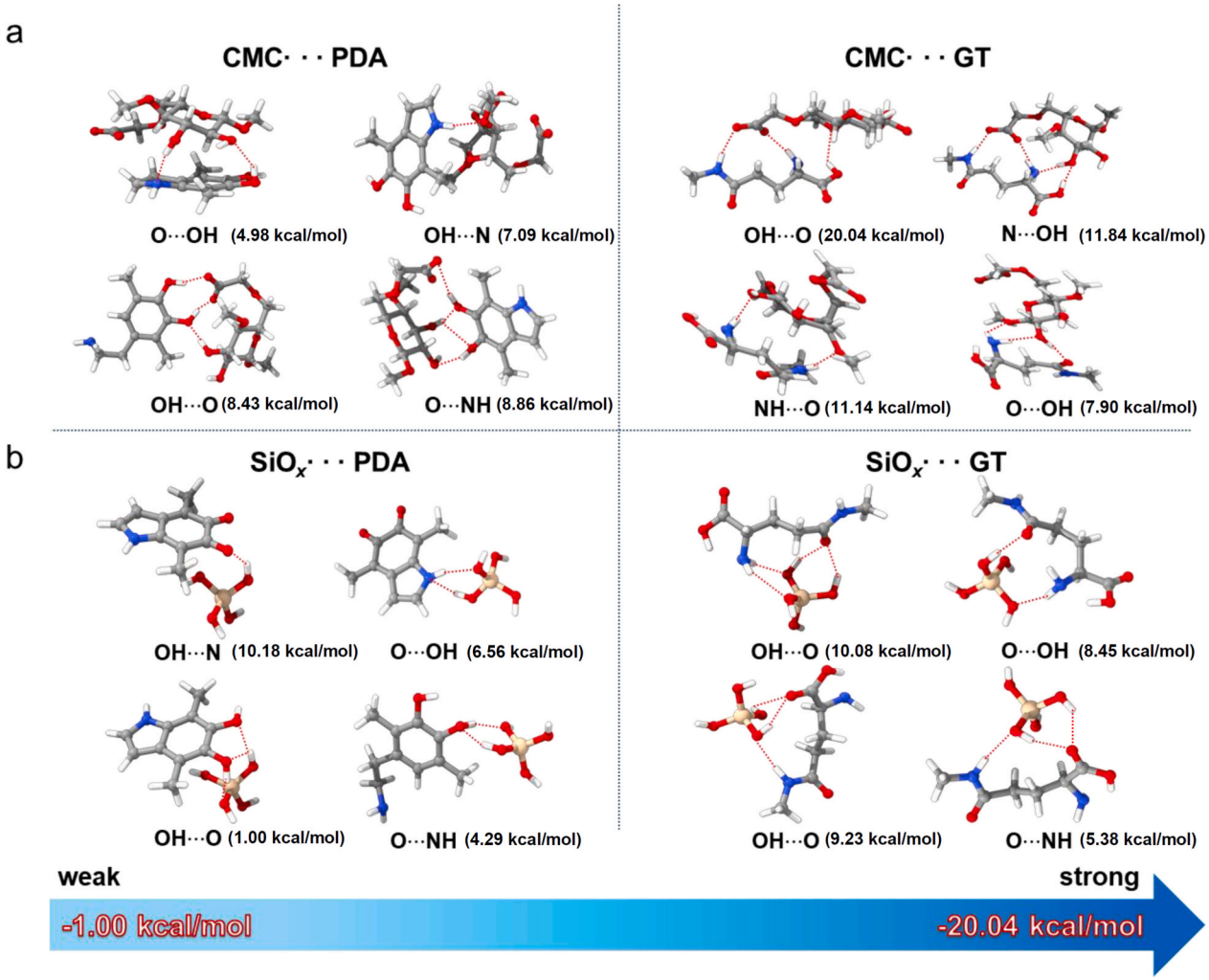


**Fig. 3.** DFT simulations for analyzing gradient hydrogen bonding of (a) CMC with PDA and CMC with GT and (b) $SiO_x$ with PDA and $SiO_x$ with GT.

formation of hydrogen bonds between the 21PDG additive and $SiO_x$ or CMC (Fig. 4a).

To further confirm the improved elasticity of the CMC–21PDG-10 binder, rotational rheometer measurements were used to analyze the changes in storage modulus (G') and loss modulus (G") with frequency for CMC–21PDG-10, and the results were compared with those for CMC (Fig. 4b). CMC–21PDG-10 exhibited a G' > G" crossover at a lower frequency than CMC. In general, the lower the crossover frequency, the higher the viscoelasticity, and the larger G' becomes than G" at high frequencies, the more elastic the polymer [57,58]. Thus, the lower crossover frequency observed for CMC–21PDG-10 indicates its more elastic behavior. Our results confirm that introducing the 21PDG additive increases the interaction with CMC and improves its limited elasticity.

### *3.6. Mechanical properties and electrochemical performance of ($SiO_x$) CMC–21PDG-10*

Nanoindentation tests were performed on ($SiO_x$)CMC–21PDG-10, the electrode fabricated using the CMC–21PDG-10 binder, to assess its mechanical properties. The results were compared with those of ($SiO_x$) CMC. ($SiO_x$)CMC–21PDG-10 showed greater hardness and a lower modulus than ($SiO_x$)CMC (Fig. 4c and d). This improvement is due to the PDA in the 21PDG additive, which enhances the adhesion and mechanical strength of the electrode while inducing the sequential dissociation of the numerous hydrogen-bonding sites with varying binding energies under external stress. This mechanism may enable the electrode to more effectively accommodate the stress caused by the volume expansion of Si.

$SiO_x$ half-cell tests were conducted on ($SiO_x$)CMC–21PDG-10 and ($SiO_x$)CMC (Fig. 5). Each electrode was fabricated at a loading level of 1.5 mg $cm^{-2}$, and the measurements were performed at a charge–discharge rate of 0.5C, following the formation cycle at 0.1C (Fig. 5a and S5).

($SiO_x$)CMC–21PDG-10 exhibited an initial Coulombic efficiency (ICE) of 83.9 %, an initial capacity of 1400.3 mAh $g^{-1}$, and a remarkable capacity retention of 72.6 % after 100 cycles. In contrast, the ICE and initial capacity of ($SiO_x$)CMC were 83.5 % and 1307.2 mAh $g^{-1}$, respectively, and its capacity retention was limited to 43.6 % after 100 cycles. To enhance these differences, the loading level was increased to 2.5 mg $cm^{-2}$ and the charge–discharge rate doubled to 1C (Fig. 5b). Under these harsher conditions, ($SiO_x$)CMC degraded after the first cycle, failing to maintain its structural integrity. In contrast, ($SiO_x$) CMC–21PDG-10 exhibited a high capacity retention of 77.6 % even after 50 cycles. This significant difference in performance is attributed to the 21PDG additive, which improves the mechanical properties of CMC (adhesion, mechanical strength, and elasticity) while increasing the number of interaction sites. These results suggest that the developed binder can effectively accommodate the volume changes of $SiO_x$ anodes and improve their electrochemical performance owing to its excellent mechanical properties.

Additionally, the rate performance of both electrodes was evaluated.

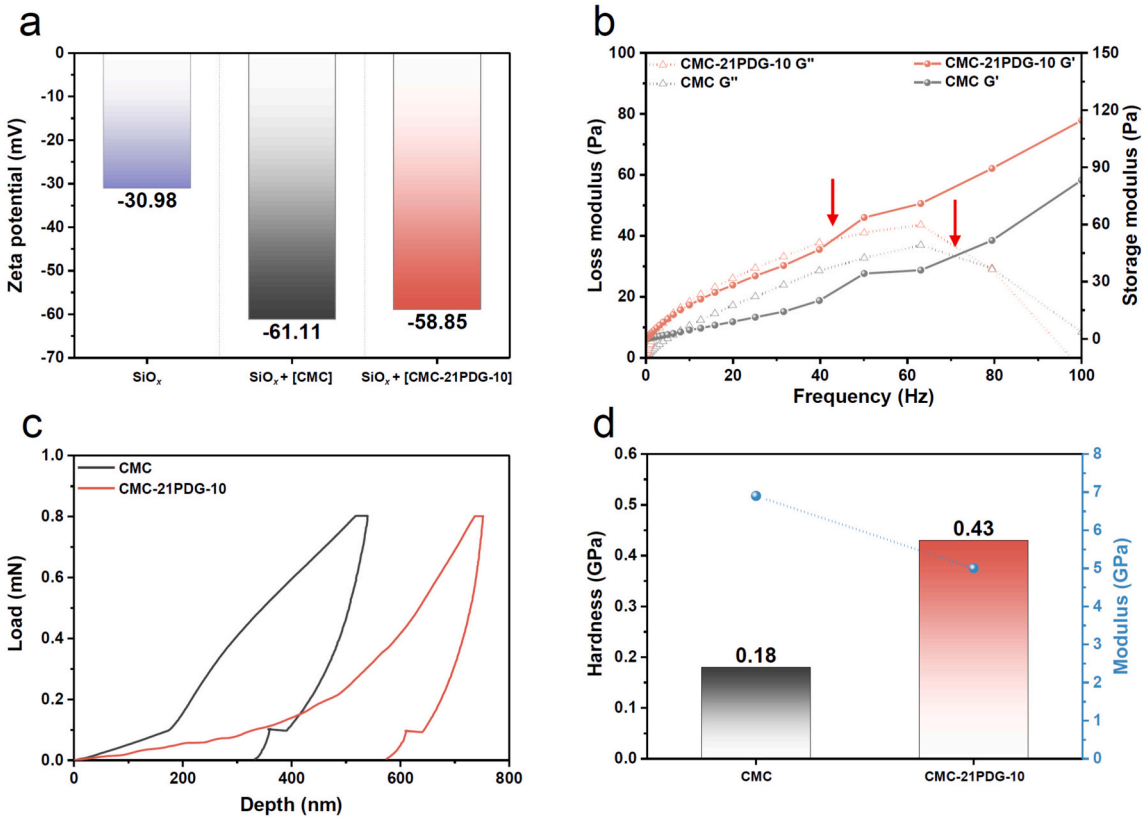


**Fig. 4.** (a) Zeta potentials of $SiO_x$, $SiO_x$(CMC), and $SiO_x$(CMC–21PDG-10), (b) rotational rheometer measurements of CMC and CMC–21PDG-10, (c) raw nano-indentation data, and (d) hardness and modulus of CMC and $SiO_x$(CMC–21PDG-10) electrodes.

($SiO_x$)CMC–21PDG-10 maintained its structural integrity even at a charge–discharge rate of 3C, demonstrating its high operational stability (Fig. 5c).

Linear sweep voltammetry and CV were conducted to assess the electrochemical stability of the CMC–21PDG-10 binder (Fig. 5d and e). The CMC–21PDG-10 binder remained electrochemically stable within the 0–3.5 V range (vs. $Li/Li^+$), as shown in Fig. 5d. The CV measurements of the binder film also confirmed its reversibility from the first to the ninth cycle, with no signs of side electrochemical reactions (Fig. 5e).

The electrochemical behavior of the electrodes was further examined using CV and EIS (Fig. 5f–5i and S6). According to the CV results, both the ($SiO_x$)CMC–21PDG-10 and ($SiO_x$)CMC electrodes maintained their structural integrity over the first 10 cycles (Fig. S6a and S6d). At the tenth cycle, the CV graph of ($SiO_x$)CMC–21PDG-10 encompassed a larger area than that of ($SiO_x$)CMC, indicating improved ion mobility in ($SiO_x$)CMC–21PDG-10 (Fig. 5f). The difference became more pronounced as the scan rate increased from 0.1 to 1.0 mV/s (Fig. S6b and S6e). As confirmed by the DMA results, this improvement is attributed to the incorporation of the 21PDG additive, which lowers $T_g$, along with the presence of PDA, whose large numbers of catechol and amine functional groups facilitate the diffusion of lithium ions.

Additionally, EIS was performed on both ($SiO_x$)CMC–21PDG-10 and ($SiO_x$)CMC (Fig. 5g–5i and S6c–S6g) [59–61]. After the formation cycle, ($SiO_x$)CMC–21PDG-10 exhibited lower electrolyte resistance and $R_{SEI}$ than ($SiO_x$)CMC (Fig. 5g). Even after 100 cycles, its resistance remained lower (Fig. 5h). This difference is attributed to the presence of PDA, which improves adhesion, along with the hydrophilic functional groups, which increase affinity with the electrolyte. These mechanisms may reduce the interfacial resistance between the electrode and the electrolyte, contributing to greater stability.

To provide further evidence for the effect of the 21PDG additive on reducing the resistance and facilitating ion diffusion, the Warburg impedance slope (σ) was calculated from the EIS data (Fig. 5i). The lower σ value in ($SiO_x$)CMC–21PDG-10 than in ($SiO_x$)CMC indicates that ($SiO_x$)CMC–21PDG-10 has a higher lithium-ion diffusion coefficient.

In addition, interfacial resistance measurements and galvanostatic intermittent titration technique (GITT) analyses were conducted. As a result, the ($SiO_x$)CMC-21PDG-10 electrode exhibited a significantly lower average interfacial resistance value of 0.173 mΩ $cm^2$ compared with 0.334 mΩ $cm^2$ for the ($SiO_x$)CMC electrode, corresponding to an approximate 48 % reduction in resistance (Fig. S7). Furthermore, the lithium-ion diffusion coefficients obtained from the GITT analysis during the lithiation and delithiation processes were compared to evaluate the average diffusion coefficient (Fig. S8). It was found that the ($SiO_x$)CMC-21PDG-10 electrode exhibited higher lithium-ion diffusion coefficient ($D_{Li}^+$) values than the ($SiO_x$)CMC electrode in both charge and discharge processes, which is consistent with the previous CV and EIS results. These findings confirm that the introduction of the PDG additive enhances both the ionic and electronic conductivity of the electrode.

Overall, introducing the 21PDG additive reduced the electrode–electrolyte interfacial resistance and enhanced the ion mobility of CMC–21PDG-10. This improvement is due to the reduced crystallinity in CMC, along with the effect of its PDA functional groups [46,62,63]. These mechanisms account for the lower electrolyte resistance and SEI resistance and the improved lithium-ion diffusion coefficient ($D_{Li+}$) of CMC–21PDG-10.

### 3.7. Morphological analysis of ($SiO_x$)CMC–21PDG-10

The surface and cross section of ($SiO_x$)CMC–21PDG-10 were analyzed using SEM before and after cycling, and the results were compared with those for ($SiO_x$)CMC (Fig. 6). Fig. 6a shows the electrode surface after 50 cycles. Even after 50 cycles, ($SiO_x$)CMC–21PDG-10 exhibited no significant cracks or defects on its surface. Active material

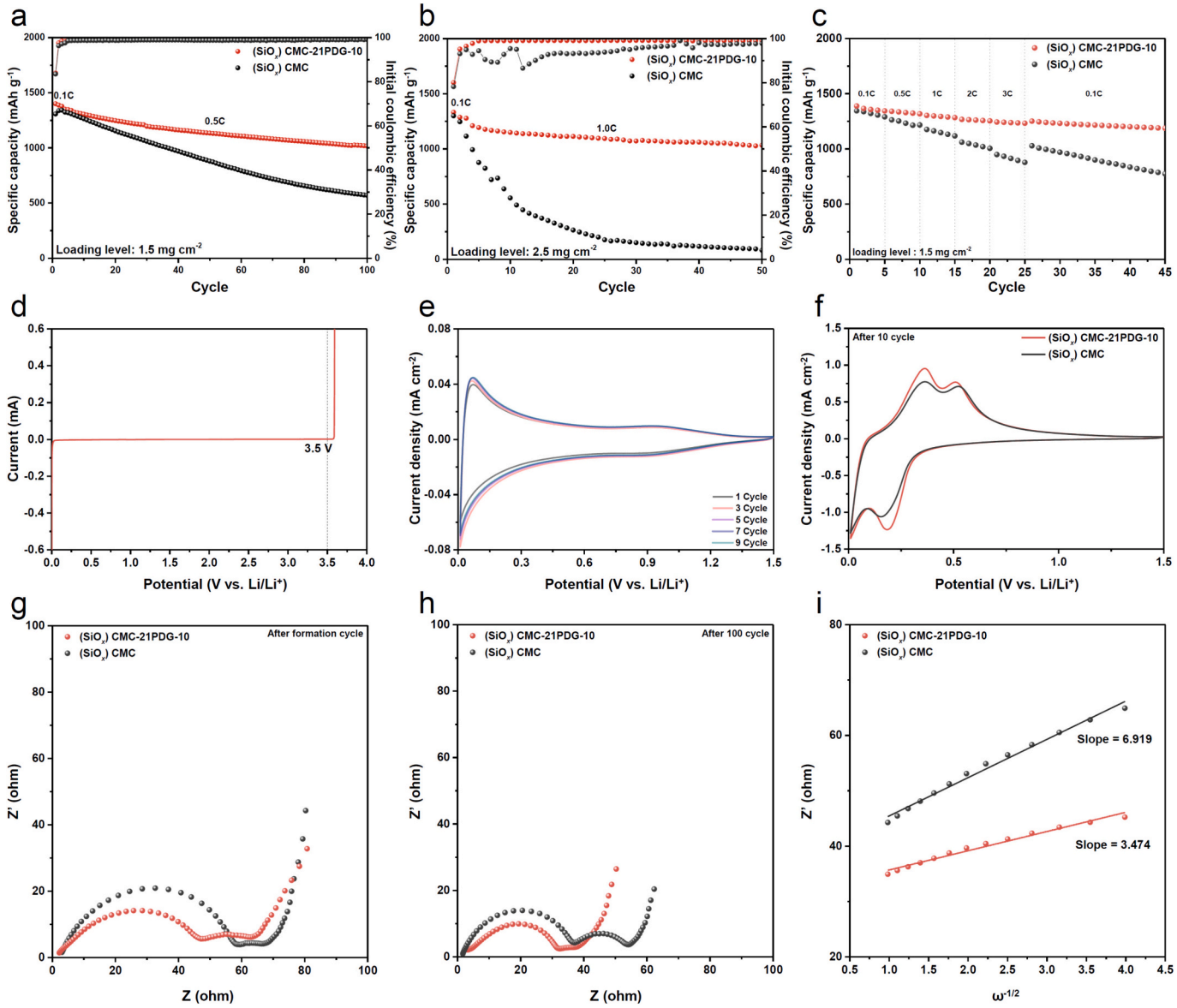


**Fig. 5.** (a) Cycling performances of ($SiO_x$)CMC–21PDG-10 and ($SiO_x$)CMC at (a) 0.5C with a loading of 1.5 mg $cm^{-2}$ and (b) 1C with a loading of 2.5 mg $cm^{-2}$, (c) rate performances at 0.1–3C, (d) linear sweep voltammogram, (e) cyclic voltammogram of the CMC–21PDG-10 binder film, (f) comparison of cyclic voltammograms of ($SiO_x$)CMC–21PDG-10 and ($SiO_x$)CMC after 10 cycles, (g and h) EIS spectra of ($SiO_x$)CMC–21PDG-10 and ($SiO_x$)CMC (g) after formation cycle and (h) after 100 cycles, (i) lithium diffusion coefficient ($D_{Li+}$) calculated from EIS Warburg impedance analysis.

particles remained visible on the electrode surface at higher magnifications, confirming the formation of thin and uniform SEI layers. In contrast, ($SiO_x$)CMC developed large and deep cracks on the surface after 50 cycles. These cracks could allow continuous permeation of the electrolyte, potentially causing electrolytic side reactions. Indeed, active material particles were difficult to discern at higher magnifications, as they were blanketed with SEI layers.

Cross-sectional morphological analysis was also conducted before and after cycling to determine the effect of the binder type on the volumetric expansion ratio of the $SiO_x$ electrodes (Fig. 6b). After cycling, the volumetric expansion ratios of ($SiO_x$)CMC–21PDG-10 and ($SiO_x$)CMC were approximately 2.1 and 2.4, respectively. Furthermore, ($SiO_x$)CMC was completely delaminated from the copper current collector after cycling. The improvements observed in ($SiO_x$)CMC–21PDG-10 are attributed to the 21PDG additive, which significantly enhanced the electrochemical performance and structural durability of the Si electrode.

### 3.8. *Electrochemical performance of (Si/C)CMC–21PDG-10 and its interaction with SBR*

The CMC–21PDG-10 binder has the greatest potential for use in $SiO_x$ active materials. To further assess its applicability, it was tested with commercial Si/C anodes, where Si is introduced into graphite. Because CMC–21PDG-10 contains PDA, it is expected to facilitate hydrogen bonding and the π–π interaction between graphite and SBR. The performance of Si/C anodes based on the CMC–21PDG-10 binder was evaluated as follows. First, the Si/C active material, binder, and Super C were combined in a ratio of 8:1:1 for electrode fabrication. The electrochemical performance of the fabricated electrode was then analyzed at a rate of 1C and compared with that of a CMC binder–based electrode fabricated under the same conditions.

The dispersion stability of the (Si/C)CMC-21PDG-10/SBR electrode was evaluated and compared with that of the (Si/C)CMC/SBR electrode. The (Si/C)CMC-21PDG-10/SBR electrode exhibited a highly uniform surface morphology, whereas the (Si/C)CMC/SBR electrode showed

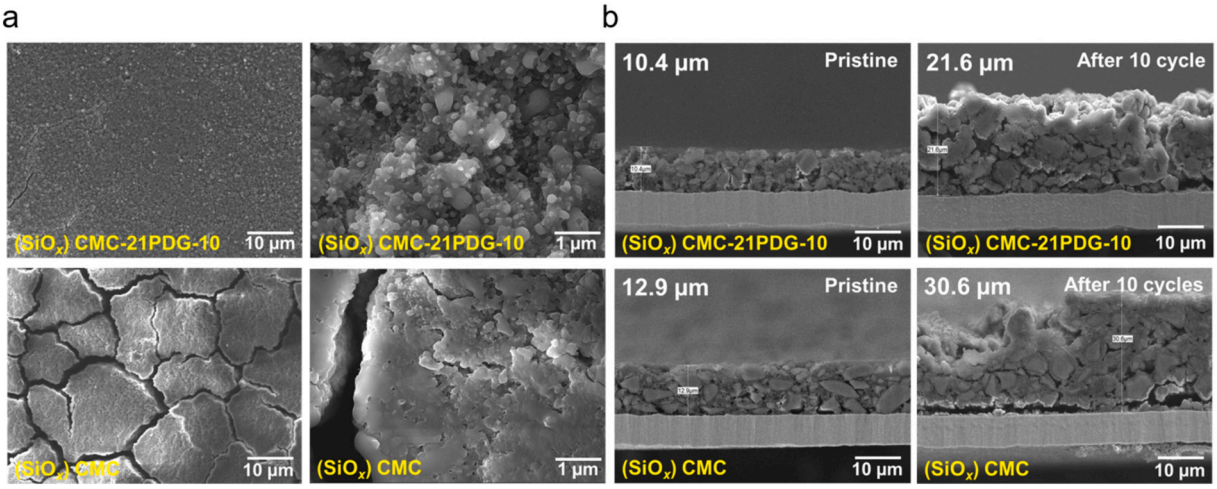


**Fig. 6.** Morphologies of ($SiO_x$)CMC–21PDG-10 and ($SiO_x$)CMC: (a) Electrode surface images after 50 cycles, and (b) Electrode cross sections after 10 cycles.

noticeable particle agglomeration on the surface (Figs. S9a and b). The dispersion stability of the electrodes was further analyzed using a 3D surface confocal laser scanning microscope (3D-LSM). The surface roughness difference of the (Si/C)CMC-21PDG-10/SBR electrode was 4.9 μm, which is lower and more uniform than that of the (Si/C)CMC/SBR electrode (6.6 μm). These results demonstrate that the developed PDG additive not only enhances π–π interactions with graphite but also strengthens interactions with SBR, improving the dispersion stability within the composite electrode (Figs. S9c and d).

(Si/C)CMC–21PDG-10 demonstrated a high initial capacity of 1361.3 mAh $g^{-1}$ and maintained an excellent capacity retention of 77 % after 100 cycles. In contrast, (Si/C)CMC had a lower initial capacity of 1232.8 mAh $g^{-1}$ and retained only 38.1 % of its capacity after 100 cycles. This improvement is attributed to the presence of 21PDG in the CMC–21PDG-10 binder, which significantly mitigates the stress caused by the volume expansion of Si while facilitating the π–π interactions with the graphite in the composite electrode. These effects were further confirmed from the results of the hydrogen-bonding simulation. Thus, the developed binder has strong potential for use in Si/C electrodes (Fig. S10a).

In addition, because commercial binders for Si/C anodes typically contain CMC and SBR, the CMC–21PDG-10 binder was modified to include SBR, and a new electrode, denoted (Si/C)CMC–21PDG-10/SBR, was fabricated using the resulting binder. Its cell performance was then compared with that of (Si/C)CMC/SBR, an electrode fabricated using a commercial CMC/SBR binder (Fig. S10b).

After 200 cycles, (Si/C)CMC–21PDG-10/SBR exhibited a capacity retention of 62.0 %, significantly higher than that of (Si/C)CMC/SBR (26.2 %). To investigate this difference, the two SBR-containing binders and pure SBR binder (CMC–21PDG-10/SBR, CMC/SBR, and SBR) were processed into films, and their mechanical properties were compared using their stress–strain curves. CMC–21PDG-10/SBR exhibited a strain more than 14 times higher than that of CMC–21PDG-10 without SBR, whereas the strain of CMC/SBR was only twice that of pristine CMC. When SBR alone was measured, a relatively low stress was observed. In contrast, the CMC-21PDG-10/SBR system maintained the inherent flexibility of SBR while exhibiting enhanced stress due to strong intermolecular interactions (Fig. S10c). These findings suggest that, as discussed above, CMC–21PDG-10 strongly interacts not only with $SiO_x$ (via hydrogen bonding) and graphite (via π–π interactions) but also with SBR (via π–π interactions).

### 3.9. Noncovalent interaction simulation for π–π interaction analysis of CMC–21PDG-10

A noncovalent interaction (NCI) simulation was conducted to investigate the interactions between PDA and graphite and between PDA and SBR to confirm that the PDA in the 21PDG additive facilitates π–π interactions between CMC–21PDG-10 and both graphite and SBR (Fig. 7) [64]. The interaction energies (dE) for graphite–CMC and graphite–PDA were − 33.0 and − 42.7 kcal/mol, respectively, with larger absolute values indicating stronger interactions. These results suggest that PDA interacts more strongly with graphite than CMC does. In NCI images, stronger NCI interactions are typically indicated by a more pronounced white semicircle [65]. This feature was more distinct for graphite–PDA than for graphite–CMC, also suggesting stronger π–π interactions. Moreover, stronger NCIs correspond to more data points in the negative region (−0.01 to −0.05) of the reduced density gradient (RDG) graph. The graphite–PDA graph exhibited a greater density of points in this region, further indicating the strong π–π interactions between graphite and PDA.

The interaction between PDA and SBR was also analyzed by NCI simulation. SBR–PDA exhibited a dE value of −19.4 kcal/mol, which had a greater absolute value than that of SBR–CMC (−8.4 kcal/mol). The white semicircle was also larger in the NCI image of SBR–PDA, and the RDG graph showed a higher concentration of data points in the negative region [66]. These results demonstrate that PDA interacts with graphite and SBR through π–π interactions.

### 3.10. Full-cell performance and SEI analysis of CMC–21PDG-10

The electrochemical compatibility of the PDG binder was evaluated in full cells with a graphite and silicon–based anode materials and a lithium nickel–cobalt–manganese oxide cathode materials (Fig. 8a and b). Although all cells exhibited similar initial capacities regardless of the binder material used the polydopamine moiety that alleviates cell polarization by enhancing the adhesion and cohesion properties at the current collector and electrode components through hydrogen bonding and π–π interactions [67]. These properties improve electronic conductivity during cycling, resulting in less polarization than in the CMC binder.

CMC–21PDG-10 also showed better cycling performance, with a capacity retention of 68.5 % after 300 cycles, compared with 57.1 % for CMC. This indicates that CMC–21PDG-10 effectively mitigates the undesired pulverization of anode materials by enhancing adhesion and cohesion. TOF-SIMS analysis of the recovered anodes supports this assumption (Fig. 8c–8f). The recovered anode with the CMC binder

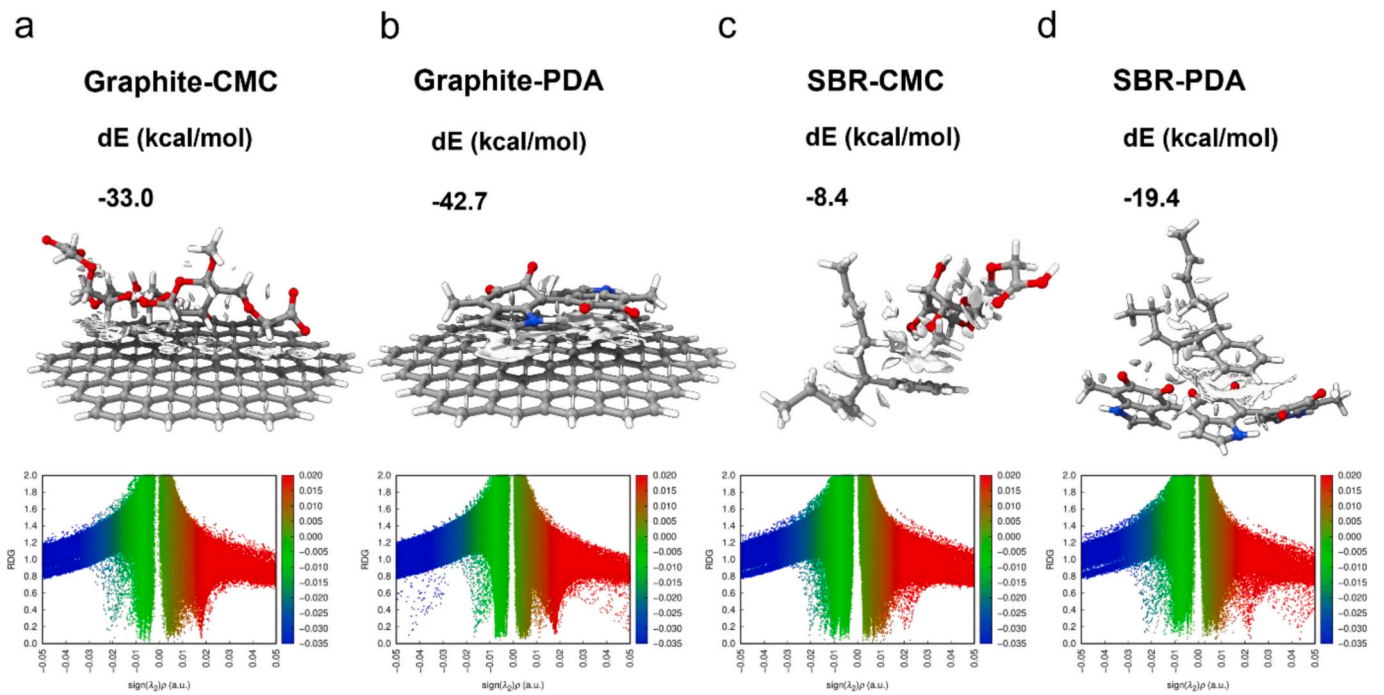


**Fig. 7.** Results of noncovalent interaction (NCI) simulation for π–π interaction analysis: (a) graphite–CMC, (b) graphite–PDA, (c) SBR–CMC, and (d) SBR–PDA.

contained high concentrations of $C_2HO^-$, $PO^-$, and $Li_2F^-$ species, which are the adducts from the solvent and lithium salt decomposition [68,69]. This suggests that the parasitic reactions resulting from the pulverization of the anode and the subsequent decomposition of the electrolyte were more severe with the CMC binder than with the CMC–21PDG-10 binder. $Li_2Si^-$, which indicates the peeled-off anode material, was also more prominent in the recovered anode with the CMC binder, suggesting more severe deformation. Notably, greater pulverization occurred in the Si-based anode, which increased the internal pressure of the cell due to accelerated electrolyte decomposition at the newly exposed interface resulting from the deformation of the anode materials [70]. To assess the impact of the binder material on cell safety, internal pressure was measured during discharge (Fig. 8g). At the end of the initial discharge, the internal pressure of the cell with the CMC binder increased to 11.38 kPa, whereas that of the cell with CMC–21PDG-10 reached only 9.05 kPa. This indicates that CMC–21PDG-10 not only increases retention by slowing anode deformation but also enhances cell safety by reducing electrolyte decomposition.

## 4. Conclusions

In this study, PDA–GT (PDG), a novel functional binder additive, was synthesized and added to CMC, a commercial polymer binder, to develop an advanced CMC–PDG binder. The polar catechol groups in PDA and the numerous hydrogen-bonding functional groups in GT enhanced the interaction with Si-based anode active materials while improving the mechanical stability of the electrode. Additionally, the multiple hydrogen-bonding functional groups in GSH sequentially dissociate during silicon anode expansion, improving electrode elasticity and alleviating stress accumulation. As a result, the developed CMC–PDG binder exhibited significantly improved adhesion and mechanical properties (hardness and modulus) compared with CMC alone.

DFT simulations confirmed the ability of PDG to form gradient hydrogen bonds with both CMC and $SiO_x$, not only mitigating stress caused by the volume expansion of Si during charge–discharge cycles but also enhancing the stability of the electrode. The optimal PDG content in CMC was 10 wt%, and the optimal monomer ratio of DA to GT for the PDG additive was 2:1. The corresponding ($SiO_x$)CMC–21PDG-10 electrode exhibited excellent capacity retention of 72.6 % after 100 cycles at 0.5C.

NCI simulations confirmed that PDG interacts with graphite and SBR through π–π interactions. Notably, the CMC–21PDG-10 binder helped maintain the structural integrity of commercial Si/C composite electrodes, ensuring their stable operation. Finally, full cells were fabricated using the CMC–21PDG-10 binder, and their performance was evaluated to assess the suitability of the binder for commercialization. A high capacity retention of 68.5 % after 300 cycles was obtained for the CMC–21PDG-10 binder-based electrode, compared with 57.1 % for CMC. The interfacial analysis of each electrode after cycling demonstrated that the CMC–21PDG-10 binder prevented electrolytic side reactions, contributing to the formation of stable and uniform SEI layers while maintaining the structural integrity of the electrode.

In conclusion, the newly developed CMC–PDG binder exhibits exceptional mechanical stability and electrochemical performance in Si-based and Si/C composite anodes. Our findings highlight the CMC-PDG binder as a cost-effective and scalable approach for developing high-performance Si-based anodes. By employing a dual-interaction strategy that leverages gradient hydrogen bonding and π–π interactions, this technology has the potential to accelerate the commercialization of next-generation high-energy-density lithium-ion batteries.

## CRediT authorship contribution statement

**Yumi Kang:** Writing – original draft, Visualization, Validation, Software, Methodology, Investigation, Formal analysis, Data curation, Conceptualization. **Ji Seong Heo:** Writing – original draft, Visualization, Resources, Methodology, Investigation, Formal analysis, Data curation, Conceptualization. **Jong Hyeok Han:** Writing – original draft, Visualization, Software, Methodology, Investigation, Formal analysis, Data curation. **Jun Won Heo:** Writing – original draft, Visualization, Software, Methodology, Investigation, Formal analysis, Data curation. **Daniel Yim:** Writing – original draft, Software, Methodology, Investigation, Formal analysis, Data curation. **Doo Ho Kim:** Visualization, Software, Methodology, Investigation, Formal analysis, Data curation. **Seo Jin Yeon:** Visualization, Software, Methodology, Investigation, Formal analysis. **Sae Chan Yoon:** Visualization, Software, Investigation,

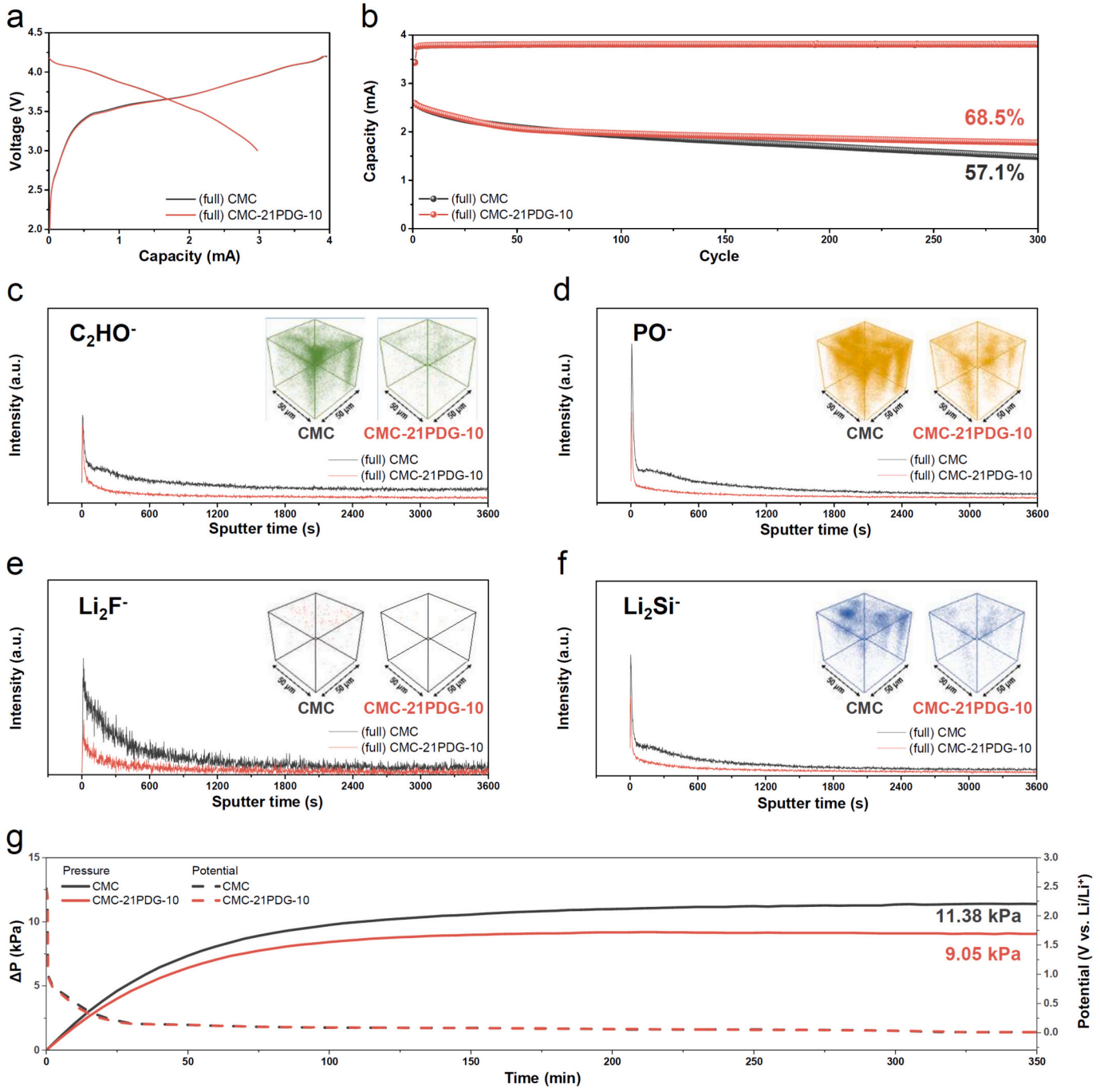


**Fig. 8.** (a) Initial voltage profile for (full) CMC and CMC–21PDG-10 cells. (b) Cycling performance for full CMC and CMC–21PDG-10 cells. (c)–(f) TOF-SIMS depth profiles and 3D reconstructions showing distribution of sputtered images for (c) $C_2HO^-$, (d) $PO^-$, (e) $Li_2F^-$, and (f) $Li_2Si^-$ with recovered anode for full CMC and CMC–21PDG-10 cell. (g) Internal pressure for CMC and CMC–21PDG-10 at the charging step.

Formal analysis, Data curation. **Hyungjun Kim:** Writing – review & editing, Supervision, Software, Resources, Project administration, Conceptualization. **Taeeun Yim:** Writing – review & editing, Supervision, Resources, Project administration, Funding acquisition, Conceptualization. **Tae-Hyun Kim:** Writing – review & editing, Validation, Supervision, Project administration, Funding acquisition, Conceptualization.

## Declaration of competing interest

The authors declare that they have no known competing financial interests or personal relationships that could have appeared to influence the work reported in this paper.

## Acknowledgments

This work was supported by the Hyundai Motors Company (development of polymer binder materials for high loading silicon composite anodes).

## Appendix A. Supplementary data

Supplementary data to this article can be found online at https://doi.org/10.1016/j.cej.2025.168879.

## Data availability

The data that has been used is confidential.

## References


[1] L. Deng, Y. Zheng, X. Zheng, T. Or, Q. Ma, L. Qian, Y. Deng, A. Yu, J. Li, Z. Chen, Design criteria for silicon-based anode binders in half and full cells, Adv. Energy Mater. 12 (2022) 2200850, https://doi.org/10.1002/aenm.202200850.

[2] A.N. Preman, H. Lee, J. Yoo, I.T. Kim, T. Saito, S.-k. Ahn, Progress of 3D network binders in silicon anodes for lithium ion batteries, J Mater Chem A 8 (2020) 25548–25570, https://doi.org/10.1039/D0TA07713E.

[3] Y. Yang, S. Wu, Y. Zhang, C. Liu, X. Wei, D. Luo, Z. Lin, Towards efficient binders for silicon based lithium-ion battery anodes, Chem. Eng. J. 406 (2021) 126807, https://doi.org/10.1016/j.cej.2020.126807.

[4] K. Feng, M. Li, W. Liu, A.G. Kashkooli, X. Xiao, M. Cai, Z. Chen, Silicon-based anodes for lithium-ion batteries: from fundamentals to practical applications, Small 14 (2018) 1702737, https://doi.org/10.1002/smll.201702737.

[5] C. Zhang, F. Wang, J. Han, S. Bai, J. Tan, J. Liu, F. Li, Challenges and recent progress on silicon-based anode materials for next-generation lithium-ion batteries, Small Struct. 2 (2021) 2100009, https://doi.org/10.1002/sstr.202100009.

[6] J.-Y. Li, Q. Xu, G. Li, Y.-X. Yin, L.-J. Wan, Y.-G. Guo, Research progress regarding Si-based anode materials towards practical application in high energy density Li-ion batteries, Mater. Chem. Front. 1 (2017) 1691–1708, https://doi.org/10.1039/C6QM00302H.

[7] S. Chae, M. Ko, K. Kim, K. Ahn, J. Cho, Confronting issues of the practical implementation of Si anode in high-energy lithium-ion batteries, Joule 1 (2017) 47–60, https://doi.org/10.1016/j.joule.2017.07.006.

[8] Y. Jin, B. Zhu, Z. Lu, N. Liu, J. Zhu, Challenges and recent progress in the development of Si anodes for lithium-ion battery, Adv. Energy Mater. 7 (2017) 1700715, https://doi.org/10.1002/aenm.201700715.

[9] H. Li, H. Li, Y. Lai, Z. Yang, Q. Yang, Y. Liu, Z. Zheng, Y. Liu, Y. Sun, B. Zhong, Revisiting the preparation progress of nano-structured Si anodes toward industrial application from the perspective of cost and scalability, Adv. Energy Mater. 12 (2102181) (2022), https://doi.org/10.1002/aenm.202102181.

[10] H. Wu, Y. Cui, Designing nanostructured Si anodes for high energy lithium ion batteries, Nano Today 7 (2012) 414–429, https://doi.org/10.1016/j.nantod.2012.08.004.

[11] M.C. Schulze, G.M. Carroll, T.R. Martin, K. Sanchez-Rivera, F. Urias, N.R. Neale, Hydrophobic versus hydrophilic interfacial coatings on silicon nanoparticles teach us how to design the solid electrolyte interphase in silicon-based Li-ion battery anodes, ACS Appl Energy Mater 4 (2021) 1628–1636, https://doi.org/10.1021/acsaem.0c02817.

[12] K. Xu, X. Liu, K. Guan, Y. Yu, W. Lei, S. Zhang, Q. Jia, H. Zhang, Research Progress on coating structure of silicon anode materials for Lithium-ion batteries, ChemSusChem 14 (2021) 5135–5160, https://doi.org/10.1002/cssc.202101837.

[13] S. Dong, L. Wang, X. Huang, J. Liang, X. He, Functionalized binders boost high-capacity anode materials, Adv. Funct. Mater. 34 (2024) 2404192, https://doi.org/10.1002/adfm.202404192.

[14] J. Yang, R. Zhao, Z. Hu, Y. Wang, K. Zhang, Y. Wang, X. Han, A. Zhang, C. Wu, Y. Bai, Blocking the passivation reaction via localized acidification and cation selective interface towards highly stable zinc anode, Energy Storage Mater 70 (2024) 103449, https://doi.org/10.1016/j.ensm.2024.103449.

[15] H. Zhao, J. Li, Q. Zhao, X. Huang, S. Jia, J. Ma, Y. Ren, Si-based anodes: advances and challenges in Li-ion batteries for enhanced stability, Electrochem. Energy Rev. 7 (2024) 11, https://doi.org/10.1007/s41918-024-00214-z.

[16] W. Dou, M. Zheng, W. Zhang, T. Liu, F. Wang, G. Wan, Y. Liu, X. Tao, Review on the binders for sustainable high-energy-density lithium ion batteries: status, solutions, and prospects, Adv. Funct. Mater. 33 (2023) 2305161, https://doi.org/10.1002/adfm.202305161.

[17] W. Jang, S. Kim, Y. Kang, T. Yim, T.-H. Kim, A high-performance self-healing polymer binder for Si anodes based on dynamic carbon radicals in cross-linked poly (acrylic acid), Chem. Eng. J. 469 (2023) 143949, https://doi.org/10.1016/j.cej.2023.143949.

[18] Y. Kang, S. Kim, J. Han, T. Yim, T.-H. Kim, Poly (acrylic acid) grafted with a Boronic Ester and Dopamine as a self-healable and highly adhesive aqueous binder for Si anodes, ACS Appl Energy Mater 7 (2024) 2436–2450, https://doi.org/10.1021/acsaem.3c03256.

[19] J.T. Wang, C.C. Wan, J.L. Hong, Polymer blends of pectin/poly (acrylic acid) as efficient binders for silicon anodes in lithium-ion batteries, ChemElectroChem 7 (2020) 3106–3115, https://doi.org/10.1002/celc.202000666.

[20] Z. Wang, T. Huang, Z. Liu, A. Yu, Dopamine-modified carboxymethyl cellulose as an improved aqueous binder for silicon anodes in lithium-ion batteries, Electrochim. Acta 389 (2021) 138806, https://doi.org/10.1016/j.electacta.2021.138806.

[21] L. Yu, B. Tao, L. Ma, F. Zhao, L. Wei, G. Tang, Y. Wang, X. Guo, A robust network sodium Carboxymethyl cellulose-Epichlorohydrin binder for silicon anodes in Lithium-ion batteries, Langmuir 40 (2024) 17930–17940, https://doi.org/10.1021/acs.langmuir.4c01151.

[22] Z. Wang, T. Huang, A. Yu, A carboxymethyl vegetable gum as a robust water soluble binder for silicon anodes in lithium-ion batteries, J. Power Sources 489 (2021) 229530, https://doi.org/10.1016/j.jpowsour.2021.229530.

[23] H. Buqa, M. Holzapfel, F. Krumeich, C. Veit, P. Novák, Study of styrene butadiene rubber and sodium methyl cellulose as binder for negative electrodes in lithium-ion batteries, J. Power Sources 161 (2006) 617–622, https://doi.org/10.1016/j.jpowsour.2006.03.073.

[24] J.H. Park, S.H. Kim, K.H. Ahn, Role of carboxymethyl cellulose binder and its effect on the preparation process of anode slurries for Li-ion batteries, Colloids Surf. A Physicochem. Eng. Asp. 664 (2023) 131130, https://doi.org/10.1016/j.colsurfa.2023.131130.

[25] A. Gupta, R. Badam, B.S. Mantripragada, S.N. Mishra, N. Matsumi, Ultra-durability and reversible capacity of silicon anodes with crosslinked poly-BIAN binder in lithium-ion secondary batteries for sturdy performance, Adv. Sustain. Syst. 9 (2025) 2400263, https://doi.org/10.1002/adsu.202400263.

[26] Z. Zheng, H. Gao, C. Ke, M. Li, Y. Cheng, D.-L. Peng, Q. Zhang, M.-S. Wang, Constructing robust cross-linked binder networks for silicon anodes with improved lithium storage performance, ACS Appl. Mater. Interfaces 13 (2021) 53818–53828, https://doi.org/10.1021/acsami.1c14907.

[27] H. Liao, N. Liu, W. He, J. Long, H. Dou, X. Zhang, Three-dimensional cross-linked binder based on ionic bonding for a high-performance SiO x anode in Lithium-ion batteries, ACS Appl Energy Mater 5 (2022) 4788–4795, https://doi.org/10.1021/acsaem.2c00221.

[28] Y. Yu, C. Yang, J. Zhu, B. Xue, J. Zhang, M. Jiang, An advanced 3D crosslinked conductive binder for silicon anodes: leveraging glycerol chemistry for superior Lithium-ion battery performance, Angew. Chem. Int. Ed. 64 (2025) e202418794, https://doi.org/10.1002/anie.202418794.

[29] D. Cheng, F. Song, Y. Zeng, D. Qin, Z. Ma, P. Zheng, G. Zhang, C. Wang, Y. Qian, Dynamic self-adaption supramolecular binder for silicon anodes: anhydride activation enabling practical lithium-ion battery, Adv. Funct. Mater. (2025) 2507041, https://doi.org/10.1002/adfm.202507041.

[30] D.-Y. Han, I.K. Han, J. Son, J.Y. Kwon, Y.S. Kim, T.K. Lee, S. Park, J. Ryu, Molecular engineering of coacervate network binders for stable silicon-based anodes in lithium-ion batteries, Adv. Funct. Mater. (2025) e09445, https://doi.org/10.1002/adfm.202509445.

[31] C. Yang, Y. Jiang, F. Chen, J. Zhao, Highly elastic hyperbranched polymer binder for silicon anodes in lithium-ion batteries, Electrochim. Acta 442 (2023) 141805, https://doi.org/10.1016/j.electacta.2022.141805.

[32] Z. Weng, S. Di, L. Chen, G. Wu, Y. Zhang, C. Jia, N. Zhang, X. Liu, G. Chen, Random copolymer hydrogel as elastic binder for the SiO x microparticle anode in lithium-ion batteries, ACS Appl. Mater. Interfaces 14 (2022) 42494–42503, https://doi.org/10.1021/acsami.2c12128.

[33] X. Wang, S. Liu, Y. Zhang, H. Wang, A.A. Aboalhassan, G. Li, G. Xu, C. Xue, J. Yu, J. Yan, Highly elastic block copolymer binders for silicon anodes in lithium-ion batteries, ACS Appl. Mater. Interfaces 12 (2020) 38132–38139, https://doi.org/10.1021/acsami.0c10005.

[34] J.-O. Kim, E. Kim, E.Y. Lim, T. Kwon, I.-J. Kim, J. Lee, J.-W. Ko, J.H. Lee, Stress-dissipative elastic waterborne polyurethane binders for silicon anodes with high structural integrity in Lithium-ion batteries, ACS Appl Energy Mater 7 (2024) 1629–1639, https://doi.org/10.1021/acsaem.3c03099.

[35] L. Tang, S. Mo, S.G. Liu, N. Li, Y. Ling, N.B. Li, H.Q. Luo, Preparation of bright fluorescent polydopamine-glutathione nanoparticles and their application for sensing of hydrogen peroxide and glucose, Sensors Actuators B Chem. 259 (2018) 467–474, https://doi.org/10.1016/j.snb.2017.12.071.

[36] M. Ohke, R. Akaishi, K. Tachibana, M. Kohri, S. Nagano, H. Ebe, J. Matsui, Janus metallic film with gold and silver luster by electroless deposition of silver using poly (dopamine acrylamide) thin film, RSC Adv. 13 (2023) 28104–28111, https://doi.org/10.1039/D3RA05099H.

[37] R. Van Der Sman, Predictions of glass transition temperature for hydrogen bonding biomaterials, J. Phys. Chem. B 117 (2013) 16303–16313, https://doi.org/10.1021/jp408184u.

[38] S. Morita, Hydrogen-bonds structure in poly (2-hydroxyethyl methacrylate) studied by temperature-dependent infrared spectroscopy, Front. Chem. 2 (2014) 10, https://doi.org/10.3389/fchem.2014.00010.

[39] T. Liu, X. Peng, Y.N. Chen, Q.W. Bai, C. Shang, L. Zhang, H. Wang, Hydrogen-bonded polymer–small molecule complexes with tunable mechanical properties, Macromol. Rapid Commun. 39 (2018) 1800050, https://doi.org/10.1002/marc.201800050.

[40] S. Zhang, K. Liu, J. Xie, X. Xu, J. Tu, W. Chen, F. Chen, T. Zhu, X. Zhao, An elastic cross-linked binder for silicon anodes in lithium-ion batteries with a high mass loading, ACS Appl. Mater. Interfaces 15 (2023) 6594–6602, https://doi.org/10.1021/acsami.2c16997.

[41] W. Wang, W. Li, S. Jing, H. Yang, H. Wang, L. Huang, Y. Mao, X. Pang, Y. Huang, L. Zhang, Quantitative lithium substitution of carboxyl hydrogens in polyacrylic acid binder enables robust SiO electrodes with durable lithium storage stability, J. Energy Chem. 97 (2024) 352–360, https://doi.org/10.1016/j.jechem.2024.05.046.

[42] X. Jiao, J. Yin, X. Xu, J. Wang, Y. Liu, S. Xiong, Q. Zhang, J. Song, Highly energy-dissipative, fast self-healing binder for stable Si anode in lithium-ion batteries, Adv. Funct. Mater. 31 (2021) 2005699, https://doi.org/10.1002/adfm.202005699.

[43] L. Hu, X. Zhang, B. Li, M. Jin, X. Shen, Z. Luo, Z. Tian, L. Yuan, J. Deng, Z. Dai, Design of high-energy-dissipation, deformable binder for high-areal-capacity silicon anode in lithium-ion batteries, Chem. Eng. J. 420 (2021) 129991, https://doi.org/10.1016/j.cej.2021.129991.

[44] D. Yao, J. Feng, J. Wang, Y. Deng, C. Wang, Synthesis of silicon anode binders with ultra-high content of catechol groups and the effect of molecular weight on battery performance, J. Power Sources 463 (2020) 228188, https://doi.org/10.1016/j.jpowsour.2020.228188.

[45] Y. Kang, J.H. Han, S. Kannan, S. Kim, S.J. Yeon, T.-H. Kim, Si anodes via dual strategies of coating Si with a rigid polymer and employing a polymer binder with

improved mechanical properties, J. Power Sources 626 (2025) 235777, https://doi.org/10.1016/j.jpowsour.2024.235777.
[46] L. Ma, S. Niu, F. Zhao, R. Tang, Y. Zhang, W. Su, L. Wei, G. Tang, Y. Wang, A. Pang, A high-performance polyurethane–polydopamine polymeric binder for silicon microparticle anodes in lithium-ion batteries, ACS Appl Energy Mater 5 (2022) 7571–7581, https://doi.org/10.1021/acsaem.2c01033.
[47] N. Liu, W. He, H. Liao, Z. Li, J. Jiang, X. Zhang, H. Dou, Polydopamine grafted cross-linked polyacrylamide as robust binder for SiO/C anode toward high-stability lithium-ion battery, J. Mater. Sci. 56 (2021) 6337–6348, https://doi.org/10.1007/s10853-020-05658-4.
[48] W. Jiang, X. Yang, J. Deng, J. Zhang, G. Zhang, Polydopamine-based materials applied in Li-ion batteries: a review, J. Mater. Sci. 56 (2021) 19359–19382, https://doi.org/10.1007/s10853-021-06536-3.
[49] S. Grimme, C. Bannwarth, P. Shushkov, A robust and accurate tight-binding quantum chemical method for structures, vibrational frequencies, and noncovalent interactions of large molecular systems parametrized for all spd-block elements (Z= 1–86), J. Chem. Theory Comput. 13 (2017) 1989–2009, https://doi.org/10.1021/acs.jctc.7b00118.
[50] C. Bannwarth, S. Ehlert, S. Grimme, GFN2-xTB—an accurate and broadly parametrized self-consistent tight-binding quantum chemical method with multipole electrostatics and density-dependent dispersion contributions, J. Chem. Theory Comput. 15 (2019) 1652–1671, https://doi.org/10.1021/acs.jctc.8b01176.
[51] D. Feller, The role of databases in support of computational chemistry calculations, J. Comput. Chem. 17 (1996) 1571–1586, https://doi.org/10.1002/(SICI)1096-987X(199610)17:13%3C1571::AID-JCC9%3E3.0.CO;2-P.
[52] L. Hu, X. Zhang, P. Zhao, H. Fan, Z. Zhang, J. Deng, G. Ungar, J. Song, Gradient H-bonding binder enables stable high-areal-capacity Si-based anodes in pouch cells, Adv. Mater. 33 (2021) 2104416, https://doi.org/10.1002/adma.202104416.
[53] D. Cheng, Y. Liu, Z. Li, T. Rao, D. Luo, P. Zheng, C. Guo, J. Wang, F. Pan, Y. Deng, An easy-to-prepare flexible 3D network aqueous binder with gradient hydrogen bonding for high-performance silicon anodes, J. Power Sources 602 (2024) 234328, https://doi.org/10.1016/j.jpowsour.2024.234328.
[54] Y. Liu, L. Wang, L. Zhao, Y. Zhang, Z.-T. Li, F. Huang, Multiple hydrogen bonding driven supramolecular architectures and their biomedical applications, Chem. Soc. Rev. 53 (2024) 1592–1623, https://doi.org/10.1039/D3CS00705G.
[55] B. Kim, Y. Song, B. Youn, D. Lee, Dispersion homogeneity of silicon anode slurries with various binders for Li-ion battery anode coating, Polym 15 (2023) 1152, https://doi.org/10.3390/polym15051152.
[56] C.-C. Li, C.-A. Chen, M.-F. Chen, Gelation mechanism of organic additives with LiFePO4 in the water-based cathode slurries, Ceram. Int. 43 (2017) S765–S770, https://doi.org/10.1016/j.ceramint.2017.05.315.
[57] J. Cho, M.-C. Heuzey, A. Bégin, P.J. Carreau, Chitosan and glycerophosphate concentration dependence of solution behaviour and gel point using small amplitude oscillatory rheometry, Food Hydrocoll. 20 (2006) 936–945, https://doi.org/10.1016/j.foodhyd.2005.10.015.
[58] X.Z. Li, S.X. Yuan, G.S. Ding, A comparative investigation of various binders for silicon anodes: interactions with other components, rheological property, and behavior in operando dilatometry, Macromol. Mater. Eng. 307 (2022) 2200376, https://doi.org/10.1002/mame.202200376.
[59] M. Ratynski, B. Hamankiewiecz, M. Krajewski, M. Boczar, D.A. Buchberger, A. Czerwinski, Electrochemical impedance spectroscopy characterization of silicon-based electrodes for Li-ion batteries, Electrocatalysis 11 (2020) 160–169, https://doi.org/10.1007/s12678-019-00573-y.
[60] W. Choi, H.-C. Shin, J.M. Kim, J.-Y. Choi, W.-S. Yoon, Modeling and applications of electrochemical impedance spectroscopy (EIS) for lithium-ion batteries, J. Electrochem. Sci. Technol. 11 (2020) 1–13, https://doi.org/10.33961/jecst.2019.00528.
[61] F. Paloukis, C. Elmasides, F. Farmakis, P. Selinis, S.G. Neophytides, N. Georgoulas, Electrochemical impedance spectroscopy study in micro-grain structured amorphous silicon anodes for lithium-ion batteries, J. Power Sources 331 (2016) 285–292, https://doi.org/10.1016/j.jpowsour.2016.09.062.
[62] Y. Zhang, X. Wang, L. Ma, R. Tang, X. Zheng, F. Zhao, G. Tang, Y. Wang, A. Pang, W. Li, Polydopamine blended with polyacrylic acid for silicon anode binder with high electrochemical performance, Powder Technol. 388 (2021) 393–400, https://doi.org/10.1016/j.powtec.2021.05.001.
[63] L. Ma, X. Fu, F. Zhao, W. Su, L. Yu, C. Lu, L. Wei, G. Tang, Y. Wang, X. Guo, High-performance carboxymethyl cellulose integrating polydopamine binder for silicon microparticle anodes in lithium-ion batteries, ACS Appl Energy Mater 6 (2023) 1714–1722, https://doi.org/10.1021/acsaem.2c03606.
[64] T. Lu, F. Chen, Multiwfn: a multifunctional wavefunction analyzer, J. Comput. Chem. 33 (2012) 580–592, https://doi.org/10.1002/jcc.22885.
[65] T. Lu, A comprehensive electron wavefunction analysis toolbox for chemists, Multiwfn, J. Chem. Phys. 161 (2024) 082503, https://doi.org/10.1063/5.0216272.
[66] J. Contreras-García, E.R. Johnson, S. Keinan, R. Chaudret, J.-P. Piquemal, D. N. Beratan, W. Yang, NCIPLOT: a program for plotting noncovalent interaction regions, J. Chem. Theory Comput. 7 (2011) 625–632, https://doi.org/10.1021/ct100641a.
[67] N. Billot, M. Beyer, N. Koch, C. Ihle, G. Reinhart, Development of an adhesion model for graphite-based lithium-ion battery anodes, J. Manuf. Syst. 58 (2021) 131–142, https://doi.org/10.1016/j.jmsy.2020.10.016.
[68] Z. He, C. Zhang, Y. Zhu, F. Wei, The acupuncture effect of carbon nanotubes induced by the volume expansion of silicon-based anodes, Energy Environ. Sci. 17 (2024) 3358–3364, https://doi.org/10.1039/D4EE00710G.
[69] L. Zheng, F. Guo, T. Kang, Y. Fan, W. Gu, Y. Mao, Y. Liu, R. Huang, Z. Li, Y. Shen, Stable lithium-carbon composite enabled by dual-salt additives, Nano-Micro Lett. 13 (2021) 1–11, https://doi.org/10.1007/s40820-021-00633-3.
[70] M. Wetjen, D. Pritzl, R. Jung, S. Solchenbach, R. Ghadimi, H.A. Gasteiger, Differentiating the degradation phenomena in silicon-graphite electrodes for lithium-ion batteries, J. Electrochem. Soc. 164 (2017) A2840, https://doi.org/10.1149/2.1921712jes.